Title

Coexistence of soft and hard magnetic phases in single layer amorphous Tb–Co thin films

Journal

Journal of Applied Physics, 131(3)

ISSN

0021-8979

Authors

Ceballos, A
Charilaou, M
Molina-Ruiz, M
et al.

Publication Date

2022-01-21

DOI

10.1063/5.0074314

Coexistence of soft and hard magnetic phases in single layer amorphous Tb-Co thin films

A. Ceballos,[1] M. Charilaou,[2] M. Molina-Ruiz,[3] and F. Hellman[1,3,4]

[1)]*Department of Materials Science and Engineering, University of California, Berkeley, California 94720, USA*

[2)]*Department of Physics, University of Louisiana, Lafayette, Louisiana 70504, USA*

[3)]*Department of Physics, University of California, Berkeley, California 94720, USA*

[4)]*Materials Sciences Division, Lawrence Berkeley National Laboratory, Berkeley, California 94720, USA*

(*Electronic mail: michalis.charilaou@louisiana.edu)

Amorphous(*a*-), ferrimagnetic Tb-Co thin films prepared with a thin Ta underlayer and either a Ta or Pt overlayer show evidence of both a soft and a hard magnetic phase. At room temperature the films exhibit conventional ferromagnetism, but low temperature magnetometry measurements reveal the decoupling of the two magnetic phases with decreasing temperature due to increased anisotropy energy of the hard layer at lower temperatures. Decreasing the film thickness to 2 nm, slightly above the superparamagnetic limit found at 1 nm, a soft, low density phase was isolated and found to be present in all the films as confirmed with x-ray reflectivity and Rutherford backscattering spectrometry measurements. For greater thicknesses, the bottom layer retains its soft magnetic nature, while the remainder of the film is denser and has strong perpendicular magnetic anisotropy, leading to exchange-spring behavior when the anisotropy becomes large, either at low temperatures or via a Pt overlayer which adds a strong interfacial anisotropy to the layer. Micromagnetic simulations of a soft/hard bilayer model with the experimentally-determined anisotropy and magnetization parameters into a soft/hard bilayer model, reproduced the experimental hysteretic behavior very well. These findings demonstrate how the magnetic state and the response of *a*–Tb-Co films to external fields can be controlled, providing a high degree of tunability that is promising for high-performance nanoscale devices.

I. INTRODUCTION

With increasing pressure for faster, denser and more energy-efficient magnetic data and logic devices comes the necessity to study reduced dimensions and interfacial phenomena in magnetism. Amongst the many magnetic materials being proposed, ferrimagnetic rare-earth (RE) - transition metal (TM) alloys have been receiving increasing attention due to their wealth of magnetic properties, situating them at the center of many proposed magnetic devices. Studies of these systems include spin-orbit torque measurements of ferro(i)magnet/heavy metal (HM) bilayer systems;[1–5] imaging of exotic spin textures such as skyrmions in multilayered HM/RE-TM alloys,[6] and ultrafast magnetization dynamics in Gd-Fe-Co and Gd-Co alloys.[7–11] All of these studies take advantage of amorphous RE-TM alloys' growth-induced perpendicular magnetic anisotropy (PMA), relatively high Curie temperature, and tunability of their magnetic properties, including the magnetic anisotropy, dipolar coupling, Dzyaloshinskii-Moriya interaction, damping and spin-orbit coupling by modifying the composition, growth temperature, anneal temperature and by engineeging the interface .[12,13] This tunability makes these systems highly desirable testbeds at the forefront of applied and basic research.

The amorphous structure of these RE-TM alloys introduces an added challenge when it comes to characterizing the structure of ultra thin films. In addition, very thin films may exhibit superparagnetic effects, and interfacial or surface effects become important and may dominate the magnetism of the film itself.

This study shows that amorphous, ferrimagnetic Tb-Co thin films, which appear to be conventional ferrimagnets at room temperature, exhibit unexpected magnetic hysteretic behavior at low temperatures, manifested in the form of magnetization steps, due to the coexistence of a low/high density bilayer that results from growth effects. This finding highlights how the growth conditions can be tuned to deliberately obtain a tailored exchange-spring type magnetic state in RE-TM thin films, which is promising for nanoscale applications.

II. GROWTH OF THIN FILMS

The thin films were deposited using a confocal DC magnetron sputtering system by co-sputtering separate Tb, Co, Ta and Pt targets. The samples consisted of trilayers of Ta(2 nm)/*a*-$Tb_{18}Co_{82}$(*t* nm)/Pt or Ta(7 nm) with *t* ranging from 2 to 16 nm for the Ta-capped samples, and 2 - 4 nm for the Pt-capped samples. All samples were grown at room temperature in 1 mTorr of Ar and a base pressure of 8×10^{-8} Torr at a growth rate of $\sim$1.0 Å/s. Samples were grown on 300 nm of amorphous silicon nitrite (*a*-SiN_x) on Si substrates, coated with 50 nm thermal oxide (SiO_2), and were determined to be amorphous via electron diffraction in a Transmission Electron Microscope.The deposition of Ta onto *a*-SiN_x ensures that the Ta underlayer is amorphous, as determined by fluctuat-ing electron microscopy[14], and it serves as an adhesion layer to enable the growth of flatter *a*-Tb-Co films[15].

The magnetic properties of the films were investigated using a SQUID magnetometer in a temperature range of 10–400 K. The layer thickness and densities were determined via X-ray reflectometry (XRR) and Rutherford backscattering (RBS). XRR measurements were conducted with a PANalytical X-Ray diffractometer (Cu-Kα radiation, 0.154 nm). The

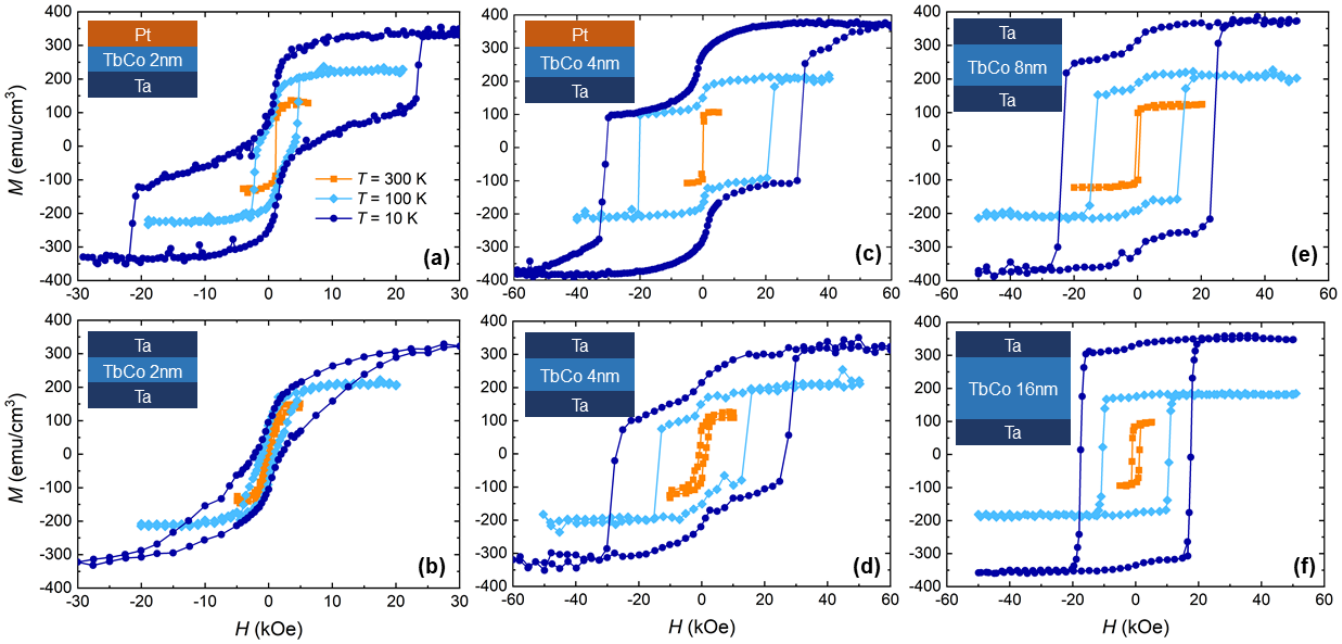

FIG. 1. Out of plane magnetization hysteresis for a-$Tb_{18}Co_{82}$ samples at room temperature (orange squares), 100 K (light-blue diamonds) and 10 K (dark-blue circles). Panels (a) and (c) correspond to the 2 and 4 nm Pt-capped samples while (b), (d), (e) and (f) correspond to the 2 – 16 nm Ta-capped samples, respectively, as shown in the inset schematics for each panel. Coercivity increases with decreasing temperature and steps are seen in all samples at 10 K except the Ta-capped 2 nm film.

RBS spectra were recorded in the Cornell geometry with a 3 MeV $^4He^+$ ion beam incident at 35° from the sample's normal and backscattered into a detector located at 165° from the incident beam direction. Higher angles of incidence were tested in order to improve the surface sensitivity but it was found that the Ta or Pt peak considerably overlapped with the Tb peak. Thus 35° was chosen as the optimal angle of incidence.

III. RESULTS AND DISCUSSION

The α–Tb-Co films' chemical composition was measured to be 18.0 ± 0.5 at.% Tb, 82 ± 1 at.% Co via RBS. At this composition the ferrimagnetic samples possess a compensation temperature of $T_{comp} \approx 150$–200 K[15]; at room temperature the net magnetization is parallel to the Co sublattice and is said to be Co-dominant, while below T_{comp} the magnetization is Tb-dominant. Figure 1 shows the out of plane (OOP) magnetic hysteresis for all samples. At 300 K every sample exhibits hysteretic behavior indicative of a homogeneous magnetic film. However upon decreasing the temperature to 100 K a step in the hysteresis is observed which is indicative of the coexistence of a decoupled soft and a hard magnetic phase. All samples exhibit this low temperature step except for the Ta-capped 2 nm film as shown in Fig. 1b. The magnitude of the step in the hysteresis is significantly reduced in the Ta-capped 8 and 16 nm samples as seen in Figs. 1e and 1f respectively. This will be shown to be associated with a soft magnetic layer that is unaffected by the total film thickness. Figs. 1a and 1c show the magnetization of the Pt-capped samples which show similar behavior to their Ta-capped counterparts. These measurements also show that the coercivity increases with decreasing temperature and that the films possess perpendicular magnetic anisotropy. The value $M_s = 100 \pm 15$ emu/cm^3 at room temperature is in good agreement to values reported in the literature for the same composition[16,17]. Importantly, the fact that all samples have the same M_s at each temperature, despite the different thickness, indicates that all films have the same composition, considering that M_s changes strongly with composition[16].

The in-plane (IP) and OOP magnetization loops of the Ta-capped 2 nm film at 10 K are shown in Fig. 2. It reveals that unlike all other samples in this study, this sample possesses no effective magnetic anisotropy as it has no preferred magnetization direction. Film thickness of 1 nm results in superparamagnetism (See Supplemental Fig. S1), and at 2 nm the film overcomes the superparamagnetic limit. However, despite achieving ferromagnetic order the sample lacks the strong PMA seen in the other samples as shown clearly in Fig. 3.

The intrinsic anisotropy constant (K_{ui}) is extracted from IP and OOP magnetization measurements using the relation $K_{ui} = H_u M_s/2 + 2\pi M_s^2$ where H_u is the anisotropy field and M_s the saturation magnetization, where H_u is determined from the external field needed to saturate the samples in the hard-axis direction. It is seen that the anisotropy is influenced by three factors: increasing film thickness increases PMA, decreasing temperature increases PMA, and capping with Pt slightly enhances the PMA. The zero effective anisotropy seen in the Ta-capped 2 nm sample is not due to K_{ui} being zero, but rather to

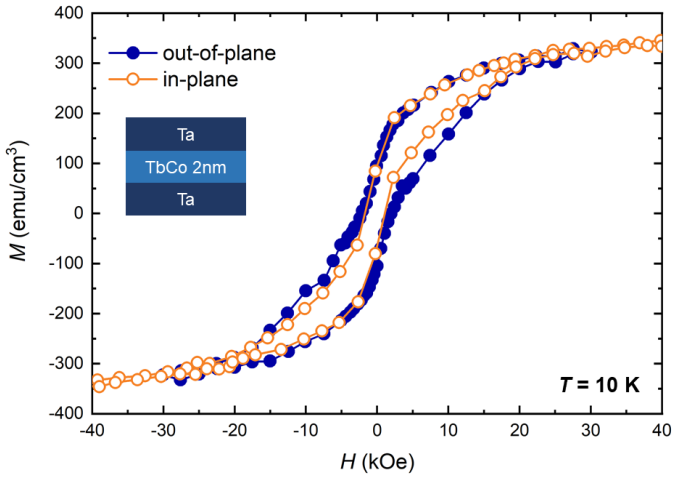

FIG. 2. Out of plane and in plane magnetization loops of the Ta-capped 2 nm sample shows no effective magnetic anisotropy, meaning that shape anisotropy is balanced by an intrinsic growth induced PMA of magnitude approximately 7×10^5 ergs/cc.

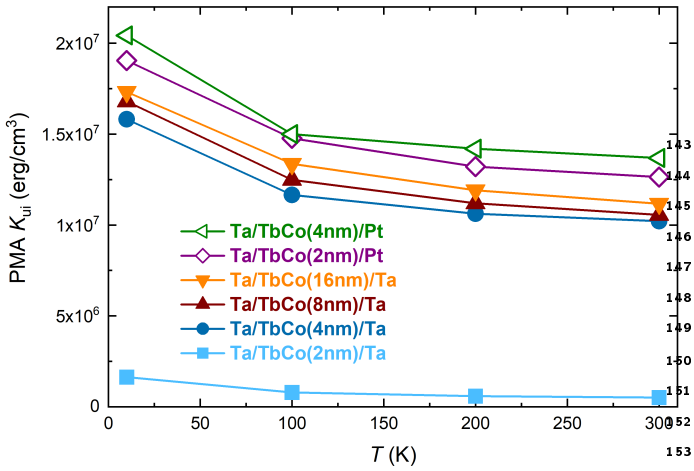

FIG. 3. Intrinsic anisotropy constant (K_{ui}) as a function of temperature. Decreasing the temperature results in increased PMA. PMA also increases with film thickness as well as by capping with Pt as seen in the Pt-capped series.

K_{ui} being very close in value to the shape anisotropy energy.

Structural characterization via XRR allows determination of sample thickness, roughness and density. XRR curves were analyzed using the GenX software,[18] in which a layered model of the samples is composed as input and the GenX program varied the thickness, roughness and density of each layer until the difference between the simulation and the experimental data was minimized. For the Ta-capped samples the layered model consisted of air/TaO_x/Ta/*a*-Tb-Co/Ta/*a*-SiN_x whereas for the Pt-capped samples it consisted of air/Pt/*a*-Tb-Co/Ta/*a*-SiN_x. Fig. 4 shows the XRR curve of the Ta-capped 4 nm sample and its accompanying simulation. Fig. 4a presents the simulation done with a single layer of *a*-Tb-Co and it is evident that it does not yield a very good fit. Fig. 4b shows the result of simulating a bilayer consisting of a lower density

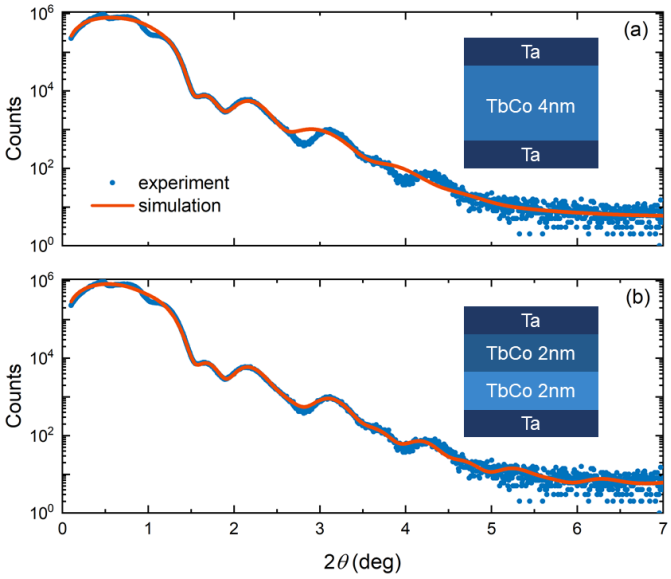

FIG. 4. XRR measurements on the Ta-capped 4 nm sample. a) Shows the inadequate fitting resulting from using a single 4 nm Tb–Co layer. b) Shows the improved fit when breaking the nominal 4 nm Tb–Co film into a bilayer of different atomic densities.

bottom layer and a higher density top layer of *a*-Tb-Co, resulting in a much improved fit. This bilayer approach had to be implemented in all films except for the 2 nm Ta-capped and Pt-capped samples in order to achieve good fits. Comparing the densities of the bottom layers across all samples revealed that the bottom layer was always ∼2 nm thick with a density that matched that of the 2 nm films as will be discussed below.

To further characterize the low/high density bilayer, the samples were probed with RBS. RBS uses MeV helium ions to depth profile information about a thin film. The helium ions recoil from classical collisions with the film's atoms, and the energy of the recoiled atoms can be modeled to tell the atomic composition and thickness or density of a thin film. Either thickness or density is required for proper RBS fitting and calculating density requires a precise measure of a film thickness which in this case is provided by the XRR analysis. Thus XRR and RBS are powerful and complementary techniques. The RBS spectra were analyzed using the SIMNRA software[19] and the densities from both XRR and RBS are plotted in Fig. 5, where the "Bottom Layer" and "Top Layer" labels denote the separate densities of the bilayer. To obtain the density from RBS the SIMNRA simulation's areal density was divided by the film thickness as extracted from XRR. The XRR bilayer thickness, roughness and density are tabulated in Table I as well as the RBS density and RMS surface roughness as measured with an atomic force microscope (AFM) as seen in supplementary materials.

The XRR data in Fig. 5 shows that a bilayer was found for all samples except the 2 nm Ta-capped and Pt-capped samples, which possess a density that is similar to that found in the initial ∼2 nm in all the other films as seen within the region labeled "Bottom Layer". Table I shows that the thickness of this lower density bottom layer is in the 1.4 - 1.8 nm range.

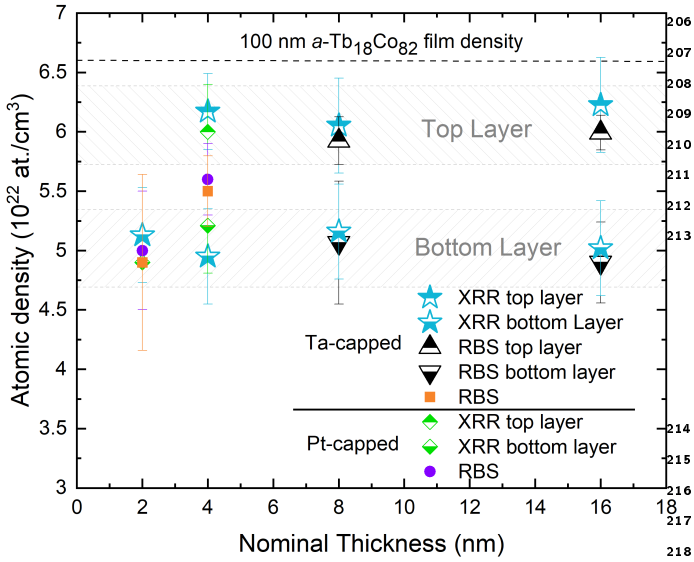

FIG. 5. Atomic density as a function of the nominal film thickness as extracted from both XRR and RBS. The rectangular regions are guides to the eyes to show the agreement of both XRR and RBS in determining the film density and confirming the bilayer model. The RBS density of the 4 nm samples lies between the two regions because it is averaging the low/high density values of the bilayer as discussed in the main text. Points labeled "RBS" indicate that a single layer was used for the fitting.

The RBS data confirmed the presence of a bilayer in the 8 and 16 nm Ta-capped samples, and a single layer fit was sufficient for the Ta-capped and Pt-capped 2 - 4 nm samples. The density extracted from RBS, is in good agreement with the density found via XRR. The RBS density found for the 4 nm samples is in between that found with a bilayer model in XRR, suggesting that a bilayer is present and its densities are being averaged in RBS. Both XRR and RBS also found a near constant density for the top layer, as seen in the gray box labeled "Top Layer" depicting a somewhat flat density trend with increasing film thickness. The dotted line at the top of Fig. 5 is the measured density of a 100 nm thick a-$Tb_{18}Co_{82}$ film, marking the density limit and showing that the density increases only slightly with increasing thickness beyond a thickness of 10 nm.

In short, these experiments show that at the growth conditions discussed in section II, amorphous Tb-Co films grow with an initial low-density layer followed by a layer that is 20% denser. The increase in density, as the film thickness increases above 2 nm, yields a bilayer system with a soft base layer and hard top layer with PMA. At room temperature, the two layers are coupled and exhibit conventional ferromagnetic hysteresis, but at low temperature they effectively decouple and the $M(H)$ curve exhibits distinct magnetization steps, the magnitude of which decreases with increasing thickness. Importantly, it should be noted that the steps in the $M(H)$ curves appear only below the ferrimagnetic compensation temperature ($T_{\rm comp}$) where the Tb moments are dominant. Considering that the magnetic moment of Tb is roughly 7 times larger than that of Co[16], the Zeeman energy becomes larger at $T < T_{\rm comp}$ therefore the soft layer follows the external field at the cost of the exchange energy between the layers. That, and the porosity found in the films, accounts for the observation of the steps in the $M(H)$ curves below $T_{\rm comp}$. In order to support this interpretation, we calculated an estimate of the external field strength required to justify the penalty in the exchange energy at the interface. The energy contributions for the soft layer can be described as

$$E = -Jx_{\rm Co}^2 S^2 - \tilde{J}x_{\rm Co}x_{\rm Tb}S\sigma - g_{\rm Co}x_{\rm Co}SB\mu_B - g_{\rm Tb}x_{\rm Tb}\sigma B\mu_B + \tilde{K}\left(x_{\rm Co}^2 S_z^2 + x_{\rm Tb}^2\sigma_z^2\right) \quad (1)$$

where S and σ is the spin of Co and Tb, respectively, J is the Co–Co exchange interaction, $\tilde{J}$ is the Co-Tb exchange interaction, g is the Landé factor, μ_B is the Bohr magneton, $\tilde{K}$ is an effective shape anisotropy due to dipole-dipole interactions, B is the external field, and $x_{\rm Co} = 0.82$, $x_{\rm Tb} = 0.18$ reflect the composition of the system. For the soft layer to rotate towards the external field, there is a penalty in the exchange interaction at the interface with the hard layer, whereas the Zeeman energy of the N atomic layers in the soft layers is satisfied, with σ in the direction of B and S in the opposite direction, i.e., ferrimagnetic order is maintained in the soft layer. This yields $B \geq Jx_{\rm Co}^2 S^2/\left(g_{\rm Tb}x_{\rm Tb}\sigma - g_{\rm Co}x_{\rm Co}S\right)\mu_B N$, and based on values from our experiments and from the literature[16] ($S = 0.7$, $\sigma = 6.0$, $J = 1\times10^{-14}$ erg, $g_{\rm Co} = 2.2$, $g_{\rm Tb} = 1.75$, $N \approx 7$), we obtain a value of $B \approx 8$ kOe, which is in reasonable agreement with the field strength at which the step in the $M(H)$ curve was observed in the experiments. At room temperature, where Co is the dominant magnetic moment, the field strength needed to rotate the soft layer becomes 28 kOe, and therefore no steps in the $M(H)$ curves would occur.

Hence, this effect is a result of the ferrimagnetic order in the films and the fact that energy contributions change with temperature as the relative sublattice magnetizations change. To further support our interpretation that the steps in the $M(H)$ curves is the result of the soft/hard layer system, we performed micromagnetic simulations.

IV. MICROMAGNETIC SIMULATIONS

In the micromagnetic continuum approximation, the total energy density in our system can be written as

$$E = A\sum_{k=x,y,z}(\nabla m_k)^2 - K_{\rm ui}(m_z)^2 - 2\pi M_{\rm s}\mathbf{m}\cdot(2\mathbf{H}+\mathbf{H}_{\rm dm}) \quad (2)$$

where $\mathbf{m} = \mathbf{M}/M_{\rm s}$ is the local magnetization unit vector, A is the exchange stiffness, $\mathbf{H}$ is the external field, and $\mathbf{H}_{\rm dm}$ is the local demagnetizing field due to dipole-dipole interactions. Hysteresis loops were simulated by sweeping the external field and minimizing the energy using the steepest conjugate gradient method in Mumax3[20].

The modeled system consists of two 40 nm by 40 nm cuboids of and a fixed thickness of 2 nm for the bottom layer to represent the low density layer, and variable thicknesses for

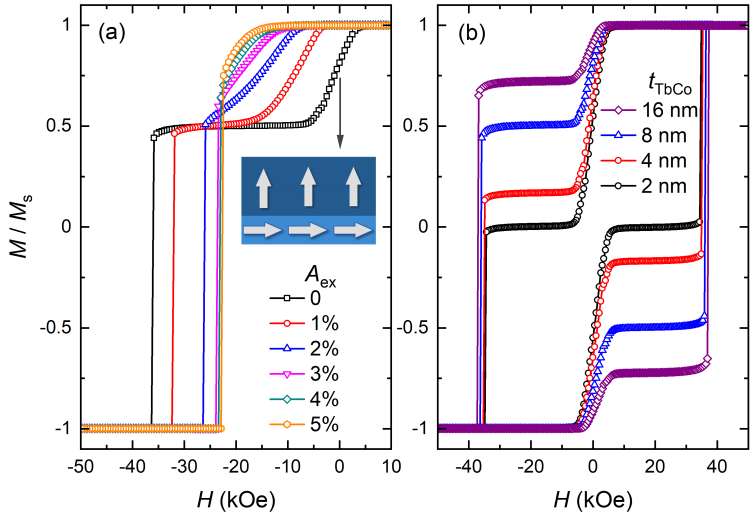

FIG. 6. Simulated magnetization reversal of a Tb-Co bilayer consisting of a soft 2 nm base layer and a hard top layer: (a) shows the $M(H)$ for a film with $t_{\mathrm{TbCo}} = 8$ nm with different strengths of the coupling between the two layers, and (b) shows the $M(H)$ loop of four different Tb-Co thicknesses, where the two layers are fully decoupled. The hysteresis loops reproduce the experimental observations.

the upper layer ranging from 2 - 16 nm. The size of 40 nm is based on the average grain size as measured via AFM on an uncapped 2 nm thick a-$Tb_{18}Co_{82}$ film as shown in supplementary materials. The two regions were modeled to have the same value of M_s = 400 emu/cm^3 (4×10^5 A/m) and exchange stiffness of $A = 2 \times 10^{-6}$ erg/cm (2×10^{-11} J/m). The layers only differed in the anisotropy constant, with the upper layer having a PMA of $K_{\mathrm{ui}} = 10^7$ erg/cm^3 (10^6 J/m^3) and the bottom layer having $K_{\mathrm{ui}} = 0$. These values were extracted from the experiments discussed above, with the exception of A, which was estimated based on the Curie temperature of the films, which was extrapolated from Ref.[16] to be $T_{\mathrm{C}} \sim 900$ K, and comparing to the values for pure Co ($T_{\mathrm{C}} = 1400$ K, $A_{\mathrm{Co}} = 2.8 \times 10^{-11}$ J/m)[21], we scaled the exchange stiffness with $A = A_{\mathrm{Co}}\,(T_{\mathrm{TbCo}}/T_{\mathrm{Co}})$. While this is only a rough estimate, it provides the correct order of magnitude. The cell size was kept at 0.5 nm, but occasional checks with different cell sizes were done to verify numerical stability.

In such a soft/hard bilayer, the exchange between the two layers plays a very important role in the magnetization reversal process. Even though micromagnetics, as a continuum approximation, cannot account for the ferrimagnetic atomistic effects discussed above, it offers a platform to investigate the effective magnetic state in such a system. As seen in Figure 6(a), which shows the simulated $M(H)$ for a film with $t = 8$ nm, when the bilayer is fully decoupled, a step occurs, similar to those observed experimentally. Specifically, as the field decreases, the magnetization of the soft layer starts decreasing before the field direction is reversed, due to the shape anisotropy of the soft layer. At zero field, the magnetization of the soft layer is in the in-plane configuration, where that of the hard layer is along the perpendicular direction, as shown by the inset to Fig. 6(a). When the field direction is reversed ($H < 0$), the magnetization of the soft layer gradually rotates towards the direction of H, and the net magnetization decreases until the field is $H = -6$ kOe, which is in good agreement to the estimate noted above. The magnetization remains nearly constant with further increasing the opposing field, until it reverses at a coercive field of -36 kOe. With increasing inter-layer exchange, the step in the $M(H)$ curve becomes smoother and with 4–5% inter-layer exchange, it vanishes completely.

Comparing these findings with the measured $M(H)$ curves shown in Fig. 1, where a step is evident and the magnetization decreases before the external field is zero, we conclude that the bilayers are effectively decoupled at low temperature. Given that, we simulated decoupled bilayer systems with different thickness of the top layer, as shown in Fig. 6(b), which again agrees with the experimental observations, i.e., with increasing thickness the magnitude of the step decreases, as the contribution of the soft layer becomes increasingly smaller.

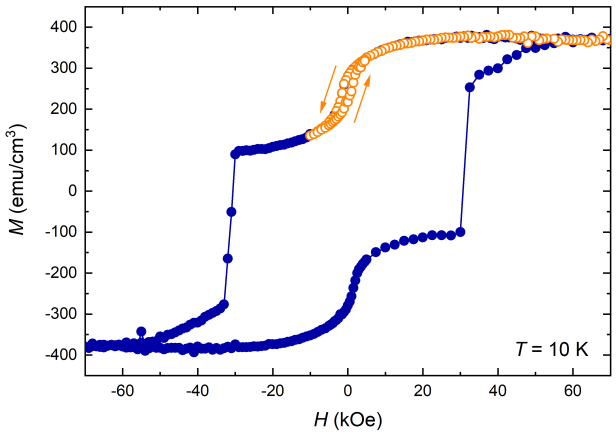

FIG. 7. Magnetization recoil curves illustrating the reversal of the soft, low density, layer of a 4 nm Pt-capped a-$Tb_{18}Co_{82}$ film at 10 K.

A soft/hard bilayer is a common recipe for exchange-spring systems which have aroused much interest in the

past two decades because of their potential in achieving giant energy products as well as their rich variety of magnetic behaviors.[22–26]. Exchange-spring systems are based on interfacial exchange coupled soft and hard ferromagnetic nanocomposites or layers, that combine the high magnetization of the soft phase with the high anisotropy of the hard phase to attain a high energy product.

Considering that the soft and hard phases are only exchange coupled at the interface, the reorientation of the soft, low density layer should be fully reversible for fields below the switching field of the hard layer. This is the namesake of the "exchange-spring" term, indicating that as long as the applied field is below that of the hard layer, the magnetization of the soft layer will spring back to orient itself with the hard phase once the field is removed. In order to confirm that the soft/hard bilayer found in the films make up an exchange-spring system, magnetization recoil curves were measured. Recoil curves are obtained from the successive removal to remanence and reapplication of an increasingly negative field from the major demagnetization. The recoil curve shown in Fig. 7 was measured on the Pt-capped 4 nm a-$Tb_{18}Co_{82}$ sample, up to an opposing field strength of -10 kOe (1 T), and illustrates that the soft layer is reversible as expected of an exchange-spring system. A minor hysteretic behavior can be seen in the recoil curve, which is attributed to grain-boundary effects. Even though other engineered structures exhibit a stronger exchange-spring effect, it is striking to observe this behavior for a single-phase amorphous metal.

The successful reproduction of the experimental hystereses via micromagnetic simulations of a soft/hard bilayer, in conjunction with the density findings from XRR and RBS, leads to the following interpretation of the growth effect: the initial 1–2 nanometers of the film grow at low density, whereas upon further growth the structure densifies, and the low/high density is responsible for the soft/hard magnetic behavior of the films. The bilayer model is an approximation of what is bound to be a more gradual change as the deposition progresses. It is very likely that this type of growth effect is present in many other systems but its effects remain hidden due to experiments at room temperature, where the anisotropy is low enough to couple both phases so the magnetization reverses coherently and often on thicker films. This model accounts for the formation of the step in all films except for the 2 nm Pt-capped, which exhibits a formidable step at low temperatures. It is quite possible that the Pt interface is responsible for the formation of the step. Since it was seen that both Pt-capped samples exhibit higher anisotropy than the Ta-capped ones, likely due to the Tb-Co/Pt interface. Thus the bilayer here would consist of soft Tb-Co and a hard Tb-Co/Pt interface. In the Pt-capped 4 nm sample, three steps are not observed because both the hard Tb-Co and the hard Tb-Co/Pt phases are close enough in anisotropy to reverse together.

V. CONCLUSION

In conclusion, the coexistence of a soft/hard bilayer in compositionally homogeneous, single layer, amorphous, ferrimagnetic Tb-Co thin films has been found to arise from a growth effect that creates a low density/high density bilayer which behaves as an exchange-spring magnet at low temperatures. This low density initial growth layer is likely a materials effect associated with nucleation of clusters in the early phase of film growth. The lower density bottom layer is magnetically soft, and for film thickness near 1 nm, the film is superparamagnetic. For film thickness near 2 nm, the film is a soft ferromagnet. For thicker films, the 2 nm thick lower soft ferromagnet continues to influence the overall magnetic properties, causing steps in the magnetic hysteresis loops at temperatures below room temperature when the anisotropy of the hard layer becomes large. XRR and RBS provided direct structural evidence of this bilayer structure for all films thicker than 2 nm. This hidden low density layer is likely present in many other material systems, but the associated soft and hard magnetic phases will decouple only when the difference in anisotropy energy is large enough, which here was enhanced by the Pt interface, typically occurring at low temperatures. These findings demonstrate how even a single phase Tb-Co thin film can exhibit exchange-spring behavior due to differences in density, and interface, and suggest that such effects might be present in a wide variety of other systems and have remained undetected. Hence, these observations suggest that growth-induced density-differential structures have the potential to yield high-performance nanoscale exchange-spring magnets.

SUPPLEMENTARY MATERIAL

See supplementary material for $M(H)$ curves of a 1 nm thick $\alpha-$Tb-Co film at $T = 300$ K and 50 K showing superparamagnetic behavior (Fig. S1), and Atomic Force Microscopy images of the Ta- and Pt-capped Tb-Co films (Fig. S2) as well as of a 2 nm un-capped film (Fig. S3).

ACKNOWLEDGMENTS

This work was primarily supported by the Director, Office of Science, Office of Basic Energy Sciences, Materials Sciences and Engineering Division, of the U.S. Department of Energy under Contract No. DE-AC02-05-CH11231 within the Nonequilibrium Magnetic Materials Program (KC2204). A.C. acknowledges support by the National Science Foundation under Grant No. DGE 1106400. M.C. acknowledges support from the Louisiana Board of Regents [contract Nr. LEQSF(2020-23)-RD-A-32].

DATA AVAILABILITY

The data that support the findings of this study are available from the corresponding author upon reasonable request.

[1]N. Roschewsky, T. Matsumura, S. Cheema, F. Hellman, T. Kato, S. Iwata, and S. Salahuddin, Appl. Phys. Lett. **109**, 112403 (2016).

[2] J.-H. Kim, D.-J. Lee, K.-J. Lee, B.-K. Ju, H. C. Koo, B.-C. Min, and O.-J. Lee, Sci. Rep. **8**, 6017 (2018).

[3] S.-G. Je, J.-C. Rojas-Sánchez, T. H. Pham, P. Vallobra, G. Malinowski, D. Lacour, T. Fache, M.-C. Cyrille, D.-Y. Kim, S.-B. Choe, M. Belmeguenai, M. Hehn, S. Mangin, G. Gaudin, and O. Boulle, Appl. Phys. Lett. **112**, 062401 (2018).

[4] K. Ueda, M. Mann, C.-F. Pai, A.-J. Tan, and G. S. D. Beach, Appl. Phys. Lett. **109**, 232403 (2016).

[5] H. W. Seung, S. Kim, D.-H. Kim, K.-J. Kim, T. Okuno, H. Yoshikawa, A. Tsukamoto, T. Moriyama, and T. Ono, Appl. Phys. Lett. **110**, 242405 (2017).

[6] R. Streubel, C.-H. Lambert, N. Kent, P. Ercius, A. T. N'Diaye, C. Ophus, S. Salahuddin, and P. Fischer, Adv. Mater. **30**, 1800199 (2018).

[7] I. Radu, K. Vahaplar, C. Stamm, T. Kachel, N. Pontius, H. A. Dürr, T. A. Ostler, J. Barker, R. F. L. Evans, R. W. Chantrell, A. Tsukamoto, A. Itoh, A. Kirilyuk, T. Rasing, and A. V. Kimel, Nature **472**, 205 (2011).

[8] C. D. Stanciu, A. Tsukamoto, A. V. Kimel, F. Hansteen, A. Kirilyuk, A. Itoh, and T. Rasing, Phys. Rev. Lett. **99**, 217204 (2007).

[9] T. Ostler, J. Barker, R. Evans, R. Chantrell, U. Atxitia, O. Chubykalo-Fesenko, S. El Moussaoui, L. Le Guyader, E. Mengotti, L. Heyderman, F. Nolting, A. Tsukamoto, A. Itoh, D. Afanasiev, B. Ivanov, A. Kalashnikova, K. Vahaplar, J. Mentink, A. Kirilyuk, T. Rasing, and A. Kimel, Nature Comm. **3**, 666 (2012).

[10] M. L. M. Lalieu, M. J. G. Peeters, S. R. R. Haenen, R. Lavrijsen, and B. Koopmans, Phys. Rev. B **96** (2017), 10.1103/PhysRevB.96.220411.

[11] J. Gorchon, C.-H. Lambert, Y. Yang, A. Pattabi, R. B. Wilson, S. Salahuddin, and J. Bokor, Appl. Phys. Lett. **111**, 042401 (2017).

[12] F. Hellman, M. Messer, and E. N. Abarra, J. Appl. Phys. **86**, 1047 (1999).

[13] F. Hellman, A. Hoffmann, Y. Tserkovnyak, G. S. Beach, E. E. Fullerton, C. Leighton, A. H. MacDonald, D. C. Ralph, D. A. Arena, H. A. Dürr, *et al.*, Rev. Mod. Phys. **89**, 025006 (2017).

[14] E. Kennedy, N. Erynolds, L. R. DaCosta, F. Hellman, C. Ophus, and M. C. Scott, Appl. Phys. Lett. **117**, 091903 (2020).

[15] A. Ceballos-Sanchez, *Characterization and manipulation of temperature-driven magnetic phenomena: magnetic transition in FeRh thin films and ultrafast magnetization reversal in* $\alpha-Gd_{22-x}Tb_xCo_{78}$ *thin films*, Ph.D. thesis, University of California, Berkeley (2019).

[16] P. Hansen, C. Clausen, G. Much, M. Rosenkranz, and K. Witter, J. Appl. Phys. **66**, 756 (1989).

[17] S. Alebrand, M. Gottwald, M. Hehn, D. Steil, M. Cinchetti, D. Lacour, E. E. Fullerton, M. Aeschlimann, and S. Mangin, Appl. Phys. Lett. **101**, 162408 (2012).

[18] M. Björck and G. Andersson, J. Appl. Cryst. **40**, 1174 (2007).

[19] M. Mayer, Germany: Garching (1977).

[20] A. Vansteenkiste, J. Leliaert, M. Dvornik, M. Helsen, F. Garcia-Sanchez, and B. Van Waeyenberge, AIP Advances **4**, 107133 (2014).

[21] A. Guimaraes, *Principles of Nanomagnetism* (Springer, 2009).

[22] E. E. Fullerton, J. Jiang, and S. Bader, J. Magn. Magn. Mater. **200**, 392 (1999).

[23] W. Si, G. P. Zhao, N. Ryan, Y. Peng, F. J. Morvan, and X. L. Wan, Sci. Rep. **5**, 16212 (2015).

[24] A. Bill and H. B. Braun, J. Magn. Magn. Mater. **272-276**, 1266 (2004).

[25] J. S. Jiang and S. D. Bader, J. Phys.: Condens. Matter **26**, 064214 (2013).

[26] J. Jiang and S. Bader, Scripta Mater. **47**, 563 (2002).

	XRR			RBS	AFM
Ta-capped	Thickness (nm) lower layer / top layer	Roughness (nm) lower layer / top layer	Density (10^{22} at/cm3) lower layer / top layer	Density (10^{22} at/cm3) lower layer / top layer	Roughness (nm)
2 nm	1.6 ± 0.3	0.64 ± 0.07	5.1 ± 0.4	4.9 ± 0.7	0.49 ± 0.07
4 nm	1.4 ± 0.3 / 2.2 ± 0.2	0.41 ± 0.08 / 0.52 ± 0.06	4.9 ± 0.4 / 6.2 ± 0.3	5.5 ± 0.3	0.45 ± 0.06
8 nm	1.6 ± 0.3 / 6.2 ± 0.2	0.47 ± 0.09 / 0.61 ± 0.08	5.2 ± 0.4 / 5.1 ± 0.4	5.1 ± 0.5 / 5.9 ± 0.2	0.39 ± 0.05
16 nm	1.5 ± 0.3 / 14.2 ± 0.2	0.39 ± 0.06 / 0.48 ± 0.07	5.0 ± 0.4 / 6.2 ± 0.4	4.9 ± 0.3 / 6.0 ± 0.2	0.54 ± 0.07
Pt-capped					
2 nm	1.8 ± 0.3	0.59 ± 0.08	4.9 ± 0.4	5.0 ± 0.5	0.41 ± 0.06
4 nm	1.4 ± 0.3 / 2.3 ± 0.3	0.42 ± 0.07 / 0.63 ± 0.08	5.2 ± 0.4 / 6.0 ± 0.4	5.6 ± 0.3	0.52 ± 0.05

TABLE I. The thickness, roughness and density of the *a*-Tb-Co bilayers as obtained from XRR. Densities obtained from RBS are consistent with those found with XRR and confirmed the presence of a low density/higher density bilayer. The RMS surface roughness measured in AFM is consistent with that obtained via XRR.